



Using true-triaxial stress path to simulate excavation-induced rock damage: a case study

Qingsheng Bai^{1,2} · Cun Zhang³ · R. Paul Young⁴

Received: 28 February 2022 / Accepted: 18 June 2022
© The Author(s) 2022

Abstract

This study presents an example illustrating the role of in situ 3D stress path method in simulating the roof damage development observed in the Mine-by tunnel at Underground Research Laboratory (URL) located in Manitoba, Canada. The 3D stress path, at the point 1 cm in the crown of the Mine-by tunnel, was applied to a cubic Lac du Bonnet (LdB) granite sample to further understand the roof damage process and the associated seismicity. After careful calibrations, a numerical model was used to reproduce the experiment, which produced similar seismicity processes and source mechanisms. Acoustic emission (AE) events obtained from laboratory and numerical modeling were converted to locations in relation to the tunnel face and were compared to the field microseismicity (MS) occurring in the upper notch region of the Mine-by tunnel. The crack development and damage mechanism are carefully illustrated. The difference between tests and field monitoring was discussed. The intermediate principal stress (σ_2) unloading process was carried out in numerical simulation to investigate its role in rock damage development. The results clearly showed σ_2 could play a significant role both in damage development and failure mode. It should be considered when predicting the damage region in underground excavations. This study highlights the potential role of laboratory and numerical stress path tests to investigate fracture processes and mechanisms occurring during engineering activities such as tunnel excavation.

Keywords Acoustic emission · Damage development · In situ 3D stress path · Numerical simulation · True-triaxial experiment

1 Introduction

The behavior of rock mass damage and failure processes are affected significantly by the stress path the rock is experienced (Bai and Tu 2019; Cai 2008b; Diederichs et al. 2004;

Kaiser et al. 2001; Wang et al. 2019; Zhang et al. 2018). Consequently, for a given condition, the evolution of damage and failure around an excavation depends on the stress path. The monotonically increased loading path, which usually applies in standard laboratory tests (such as uniaxial or triaxial compression), may not represent in situ conditions. Underground excavations not only produce stress loading in the rock mass but also unloading near the excavation boundaries, where rock fracturing and failure usually occur (Cong et al. 2020; Zheng et al. 2017). Also, we cannot relate the laboratory results to the in situ conditions because laboratory results are obtained from a different stress state and history from the in situ environment.

Stress path tests or simulations have previously been used to help understand excavation-induced rock damage. In numerical simulations, Cai (2008b) reported the deformation and yielding zone near the excavation surface, which is closely related to the unloading rate that was used to simulate the excavation. Using Discrete Element Method (DEM) models, Li et al. (2014) investigated how the unloading rate

✉ Qingsheng Bai
qingsheng_bai@yahoo.com

✉ Cun Zhang
cumt-zc@cumt.edu.cn

¹ State Key Laboratory of Coal Mine Disaster Dynamics and Control, Chongqing University, Chongqing 400044, China

² Geotechnical Institute, TU Bergakademie Freiberg, Gustav-Zeuner-Straße 1, 09599 Freiberg, Germany

³ School of Resource and Safety Engineering, China University of Mining and Technology (Beijing), Beijing, China

⁴ Department of Civil and Mineral Engineering, University of Toronto, Toronto, Canada

and initial stress release path affect the deformation, damage, and kinetic energy evolution during a circular tunnel excavation. In a detailed three-dimensional finite-element study, Eberhardt (2001) demonstrated the evolution of near-field stress paths during the progressive advancement of a tunnel face. In the study, the emphasis was placed on the rotation of the principal stress and its effect on microfracture initiation and propagation, brittle fracture damage, and rock strength degradation. In field simulations, Diederichs et al. (2004) employed an excavation-induced stress path to explain how the near-face stress rotation affects the in situ strength degradation and the damage development. Field measured and predicted stress paths were used by Kaiser et al. (2001) to explain the nature of different failure modes in an underground mine.

To capture the realistic rock mass responses, the stress path should be correctly represented in a test or model. Several studies have conducted stress path tests to simulate in situ problems. Ivars et al. (2011) illustrated an example of predicting block caving fragmentation by applying the mining-induced stress path to SRM (synthetic rock mass) models. Zhang et al. (2016) presented the results of mechanical and permeation properties on coal samples under the mining-induced stress path and found the stress-dependent permeability agrees well with field measurements. Still, the results are quite different from those of the conventional triaxial tests under monotonic loading regimes. Recently, a series of experiments were conducted using an in situ 3D stress path (Nasseri et al. 2016) to understand the strength, deformation, and seismic response during the Posiva's Spalling Experiment (POSE). The experiment makes it possible to accurately obtain the rock responses (e.g., strength, deformation, damage process, etc.) using intensive monitoring systems in a laboratory environment but under an in situ stress state. The experiments on the homogenous pegmatite

have shown the calculated P -wave velocities during the stress path tests were in reasonable agreement with those measured in the field (Young et al. 2020). The research also highlighted σ_2 plays a vital role in the damage of the veined rocks under some circumstances, indicating the characteristics of mechanical behaviors concluded in these tests cannot be replicated with conventional triaxial testing where $\sigma_2 = \sigma_3$.

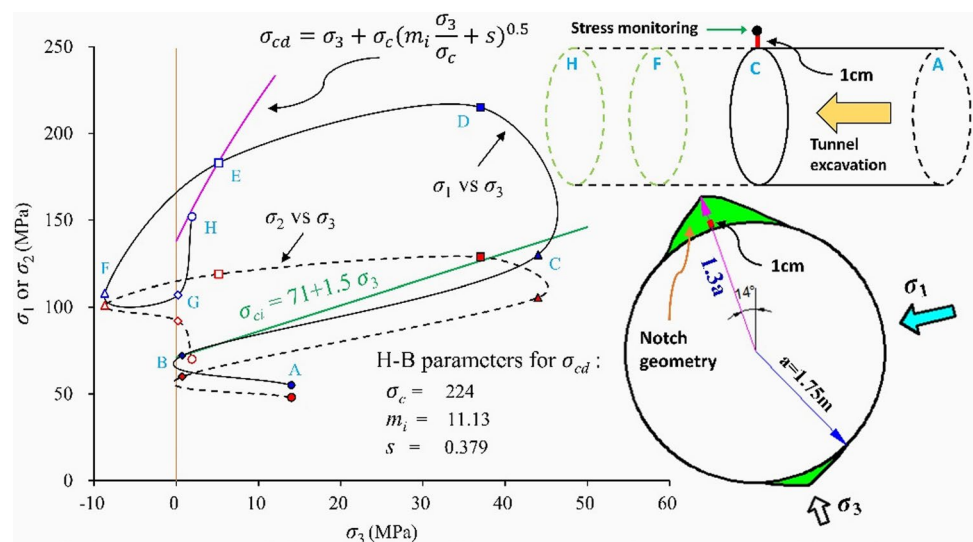
This paper presents a further investigation by applying the in situ 3D stress path to a sample to simulate the roof damage process of the Mine-by tunnel. With this approach, the damage process during the excavation of the tunnel can be examined directly in the laboratory experiment and numerical simulation, something generally difficult to obtain in conventional triaxial experiments and numerical simulations. The comparison with the field observations on the damage development, seismicity, and fracture mechanism verifies the validity of this method.

2 Methodology

2.1 Stress path at the crown of the Mine-by tunnel

The Mine-by tunnel was designed to investigate damage development around a circular tunnel in a highly stressed rock mass. It has been analyzed and well documented by numerous researchers (Martin et al. 1997; Martin 1997; Read et al. 1998). The stress path for a point of 1.0 cm from the tunnel crown as the tunnel develops was calculated using a FLAC3D model (Bai et al. 2019). Eight tunnel face locations in relation to the monitoring point, A (7 m), B (0.26 m), C (0.013 m), D (-0.013 m), E (-0.038 m), F (-0.063 m), G (-0.138 m) and H (-10 m), are used to mark the character of the stress path. The conceptual model is shown in Fig. 1. The simulated stress was also verified with field

Fig. 1 Stress paths (σ_1 - σ_3 and σ_2 - σ_3) at the location of 1.0 cm from the tunnel crown with the eight key tunnel face locations. The crack initiation strength (σ_{ci}) (Martin 1997) and crack damage strength (σ_{cd}) (Martin 1997) using fitted Hoek-Brown (H-B) failure criterion are also given in the figure. A conceptual model to obtain the stress path is shown. The notched failure profile of the Mine-by tunnel is illustrated



measurements (Martin 1997) at radial distances of 2.65 m and 3.34 m (Bai et al. 2019). Velocity measurements during the experiment were equated with the in situ results at similar stress states (Tibbo 2018) and showed the stress path experiment was simulating this parameter during the tunnel excavation process.

The stress path (σ_1 - σ_3 , and σ_2 - σ_3 plots) is shown in Fig. 1 according to the eight reference locations. There are some points of interest in this plot. σ_1 exceeds the crack initiation strength (σ_{ci}) at point B, which means cracks initiate in front of the tunnel face. However, at the area immediately in front of the tunnel face (point C), both σ_1 and σ_2 are below σ_{ci} . At the location directly behind the tunnel face (point D), stress levels for both σ_1 and σ_2 are above the σ_{ci} but much smaller than the crack damage strength (σ_{cd}) proposed by Martin (1997). After that, the minimum principal stress approaches tensile (point F) and reaches the level of the tensile strength of the LdB granite (9.3 MPa) (Martin 1997). Then σ_3 increases and becomes compressive at a location 0.16 m behind the face (point H). Meanwhile, σ_1 increases and reaches σ_{cd} .

Since tensile stress cannot be applied to the sample in the true triaxial test (TTT), the minimum magnitude of σ_3 was set to 2 MPa (e.g., σ_3 at points B, F, G, and H is 2 MPa) to maintain a functional coupling between AE transducers and loading platens (Nasseri et al. 2014). The applied stress path in the TTT is summarized in Table 1. The same stress path was used in the numerical modeling.

2.2 Numerical modeling

Compared with continuum methods, the Discrete Element Method (DEM) explicitly simulates crack initiating and propagating from microscale to macroscale without applying

complex constitutive laws. This advantage makes it widely used to observe cracking and failure in brittle rocks. The Parallel Bond Model (PBM) (Potyondy and Cundall 2004) has been successfully used to simulate failure processing of brittle rocks both in laboratory tests and field practice (Potyondy 2015; Wang and Tonon 2009; Xu et al. 2020) and the effects of heterogeneity and anisotropy on rock behaviors (Duan and Kwok 2016; Peng et al. 2017; Tian and Yang 2017). However, three inherent problems are encountered when using this model (Cho et al. 2007; Potyondy and Cundall 2004): (1) the unrealistic low ratio of uniaxial compressive strength (UCS) to tensile strength, (2) the excessively low friction angle, and (3) the linear strength envelope. The unrealistic microstructure features used in the PBM model are recognized as one of the primary reasons causing these intrinsic problems (Cho et al. 2007; Wu and Xu 2016). The irregular bonded grains in the real rock are simplified mimicked as spheres (or circular disks in 2D) in the BPM, which may not adequately reflect the geometry-dependent interlocking that does not fully mobilize the frictional strength between particles (Bahrani et al. 2011; Potyondy 2010). In BPM, contacts between particles are bonded across their entire length. After bond breaks, they are removed and lose the ability to resist relative rotation (Potyondy 2012), which underestimates the internal frictional strength (Wu and Xu 2016).

To overcome the inherent problems, the Flat-Joint Model (FJM) was proposed (Potyondy 2012). In the model, well-connected intergranular interlocks between rigid grains are produced by assigning an appropriate initial surface gap. The FJM provides the behavior of a finite-size, linear elastic, and either bonded or frictional interface. The interface is discretized into elements and can be deformable, breakable, and partially damaged. The interface evolves from a fully bonded state to a fully unbonded and frictional state.

Table 1 Stress path used in the TTT and numerical modeling

Stage	Principal stress (MPa)			Deviatoric stress (σ_1 - σ_3)	Location to the face (m)	Referencing to stress paths	AE
	σ_1	σ_2	σ_3				
1 (In situ state)	2	2	2	–	7.0	–	–
	14	14	14				
	48	48	14				
	55	48	14				
2	72	60	2 (0.7) ^a	70	0.26	B	–
3	130	106	44	86	0.013	C	90 (6)
4	215	128	37	178	–0.013**	D	1654 (423)
5	183	119	2 (5.2) ^a	181	–0.038	E	634 (209) ^b
6	108	101	2 (–8.7) ^a	106	–0.063	F	561 (147)
7	107	92	2 (1.3) ^a	105	–0.138	G	567 (74)
8	152	70	2	150	–10.0	H	521 (45)

**Negative values mean the tunnel has passed (Fig. 1). ^aReal stresses in the brackets were replaced by 2 MPa in the laboratory and numerical tests. ^bNumber of events within the sample.

Partially damaged interface, even a fully broken interface, continues to resist relative rotation because the flat joint is not removed (Potyondy 2012). Besides, pre-existing cracks and open-pores can also be presented in the microstructure of a flat-jointed material by introducing a unbonded slit and unbonded gapped contacts, respectively (Potyondy 2017). Details of the model formulation, behaviors, force–displacement laws, and failure criterion can be found in Itasca Consulting Group Inc (2017) and Potyondy (2012, 2017).

In PFC, each bond contact breakage forms a microcrack and releases part of the stored strain energy in the form of a seismic wave (Al-Busaidi et al. 2005; Hazzard and Young 2002, 2004). The released strain causes the change of the contact forces around the breakage, which can be used to calculate the moment tensor of the acoustic emission (AE) (Hazzard and Young 2004). In reality, slipping on existing joints or faults would also produce seismicity (e.g., natural earthquakes); however, slipping on failed contacts (i.e., crack slipping) is not regarded as an AE event in this numerical study. Individual AEs should be clustered into large ones to obtain realistic magnitude distributions. AEs that fall within a specific space window and their duration (time window, i.e., computational time step in the PFC code) overlap are considered part of a larger event. The space window (SW) and time window (TW) for clustering affect the size of events and the distribution of event magnitudes (Bai et al. 2021; Khazaei et al. 2015b). Therefore, SW and TW should be properly calibrated to obtain realistic results.

3 Experimental results

The 3D stress path (listed in Table 1) was applied to a cubic LdB granite sample, which was drilled from the nearby location of the Mine-by tunnel, to simulate the roof damage development. The experiment has been previously described in Bai et al. (2019). In this study, the seismic data were further processed to obtain the complete AE time-series by revisiting the continuously recording waveforms (Young et al. 2013), which had not been reported in the previous study (Bai et al. 2019).

In the former analysis (Bai et al. 2019), 308 AE were recorded based on the triggered system. In this study, the continuous waveforms identified 4027 AEs. Due to the complex velocity structure during the experiment, 904 AEs were successfully located within the specimen. A plot of the magnitude distribution for the located AEs is shown in Fig. 2. The b -value was estimated using the maximum likelihood method (Aki 1965) and considering the binning correction (Amorèse et al. 2010):

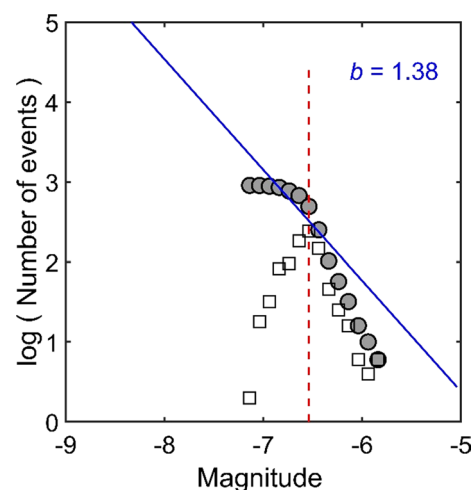


Fig. 2 Frequency-magnitude distribution (FMD) plot for AE events showing a b -value of 1.38. Filled circles are the cumulative number of AE, and hollow squares are the non-cumulative number of AE. The dashed vertical line and straight blue line indicate the magnitude of completeness and the estimated Gutenberg–Richter relation (Gutenberg and Richter 1944), respectively. Note the low estimation quality due to the gradually curved FMD

$$b = \frac{\log_{10}(e)}{\langle m \rangle - (m_c - 0.5\Delta m)} \quad (1)$$

where m_c is the magnitude of completeness, which is defined as the lowest magnitude above which all seismic events within a certain region are reliably detected (Woessner and Wiemer 2005); $\langle m \rangle$ is the mean magnitude with $m \geq m_c$. $\Delta m = 0.1$ is the magnitude bin size. A correct estimate of m_c is crucial to calculate the b -value. We assess m_c by using the maximum curvature method (Wiemer and Wyss 2000). In this experimental test, the slope of the frequency-magnitude plot (b -value) is 1.38.

In the first 3 stages (see Table 1), few AE events occurred. 423 AEs occurred in the top left part of the sample in Stage 4, as shown in Fig. 3a. Additional 209 AEs formed at Stage 5 (see Fig. 3b). In Stages 6, 7, and 8, a total of 266 AEs were recorded within the sample. Most of these events are located in the same region as that formed in Stages 4 and 5, indicating microcracks propagated along the existed cracks that formed in the former stages. The AE cloud determined a damage plane using the best fitting method described in Ingraham et al. (2013). The damage plane orientates 34° from the σ_1 direction (approximately paralleling to σ_2 , 4°), which is consistent with the previous analysis (Bai et al. 2019).

The stress path (Table 1) used in the TTT produced a potential damage plane, but the sample did not fail, which is not consistent with the field observations. Monitoring in the field showed that microseismic events initiated 0.5–1.0 m ahead of the tunnel face (stress path B and C or Stage 2

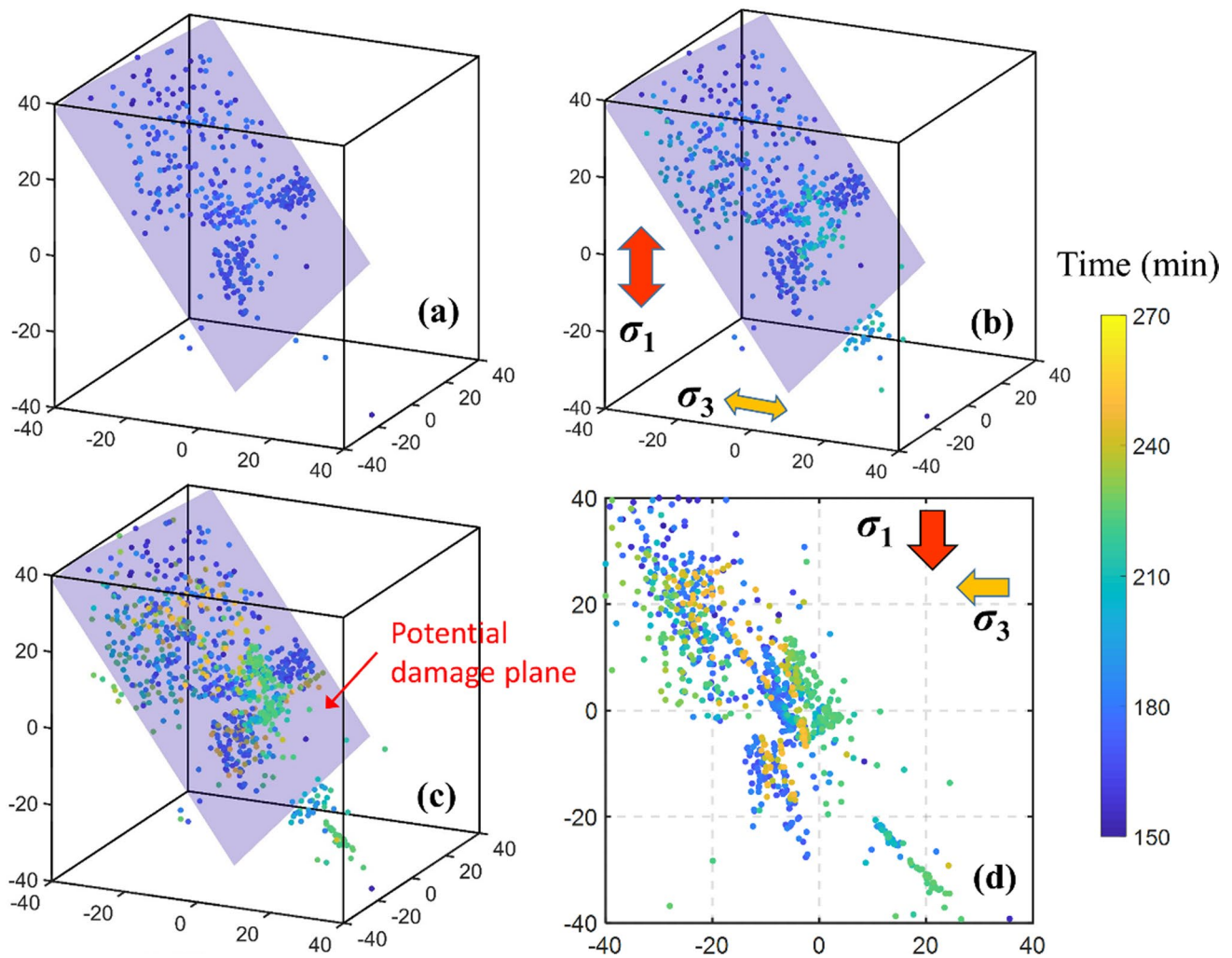


Fig. 3 Cumulative AE locations in **a** Stage 4, **b** Stage 5, **c** Stage 8, and **d** the projection in σ_1 – σ_3 plane. Events are colored according to time (cold color for early occurrence and hot color for later occurrence)

and 3, see Table 1). Microcracks propagated and coalesced into small-scale flaking and then resulted in thin slabs in the area approximately 0.5–1.0 m behind the tunnel face. The slabs progressed in an unstable manner with larger slabs and finally produced stable notches in the roof and floor (Martin et al. 1997; Martin 1997), as shown in Fig. 1. It is likely that the modified σ_3 used in the TTT contributed to the disagreement between field observation and the experiment (Bai et al. 2019). Field observations show that damages around the tunnel were susceptible to confining stress (Read and Martin 1996). However, tensile stress and low compressive stress were replaced by a confining pressure of 2 MPa (see Table 1), which should be provided to make efficient contact between AE sensors and the sample. Therefore, the modified stress path listed in Table 1 cannot fully reflect the real manner of the field conditions, although similar stress paths

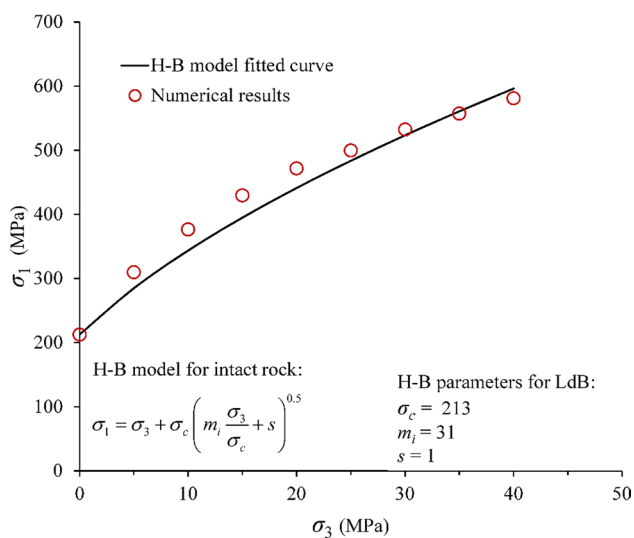
(not include the tensile part) were widely used to explain the notch formation of the Mine-by tunnel, e.g., Diederichs et al. (2004), Li et al. (2017) and Martin (1997).

4 Numerical model calibrations

The numerical model is calibrated to present the macro properties of the LdB granite. Numerical calibrations were conducted on cylinder samples with a size of 50 mm in diameter and 125 mm in length. The sample consists of approx. 9400 particles. Table 2 summarizes the calibrated microparameters for the LdB granite. The calibration results are illustrated in Fig. 4. The simulated strength envelope is nonlinear and is consistent with the H–B failure criterion (Read et al. 1998). The numerical results are also summarized in Table 3 and compared with laboratory results and the H–B model.

Table 2 Calibrated microparameters for LdB granite

Microparameter	Value
Minimum particle radius, R_{\min} (mm)	1.15
Maximum to minimum particle radius, R_{\max}/R_{\min}	1.66
Particle density, ρ (kg/m ³)	2560
Installation gap, g_i (mm)	0.4
Bonded element fraction, φ_B	0.9
Gapped element fraction, φ_G	0.0
Gapped element fraction, φ_S	0.1
Elements in radial direction, N_r	1
Elements in circumferential direction, N_a	3
Effective modulus of particle and bond, $E_c = \bar{E}_c$ (GPa)	78.0
Contact normal to shear stiffness ratio of particle and bond, $k_n/k_s = \bar{k}_n/\bar{k}_s$	1.9
Mean and standard deviation bond tensile strength, σ_{bt} (MPa)	(15.5, 0)
Mean and standard deviation bond cohesion strength, σ_{bc} (MPa)	(310, 62)
Friction angle for bonded contacts, ϕ (°)	20
Friction coefficient for failed contacts, μ	0.2

**Fig. 4** Comparison of the simulated results with the H-B failure criterion given by Read et al. (1998)

The results reveal that the errors between the laboratory properties and the simulated values are within $\pm 10\%$.

The UCS test produced shear failure with the primary fracture traveling through the sample with an angle of approx. 60° , as shown in Fig. 5a. Most of the larger AE events concentrated along the failure plane. The crack initiation (σ_{ci}) agrees well with the onset of microcracks and AE events, as shown in Fig. 5b. This phenomenon is consistent with laboratory results (Eberhardt et al. 1998; Martin 1993).

The axial stress sharply decreased after the peak value with a quick increase of AE events (Fig. 5c). Therefore, the FJM used in the study successfully reproduced the brittle failure of the LdB granite.

The space window (SW) of 2 times averaged particle diameter is suggested (Hazzard and Young 2004; Yoon et al. 2015) to calculate the AE moment tensor in the PFC model. The time window (TW) was determined by calculating the b -value using different TWs, as shown in Fig. 6. It can be seen the 30 and 40 TW produced a huge event with a magnitude of -4.5 and a source dimension of 5.1 cm, which clustered most of the microcracks near the failure plane, so there are few events along the failure plane. There is also a large magnitude gap between the largest and the second-largest events (see Fig. 6). Such a large event is unrealistic and is quite different from laboratory experiments. Laboratory tests showed a large number of AEs always spatially aligned on primary fractures (Lockner et al. 1991; Sellers et al. 2003). Events in 10 TW were smaller than -5.7 and therefore generated a larger b -value of 1.56. The 20 TW produced more realistic AE behaviors (see Fig. 5), and the b -value agrees well with laboratory results which are near unit for hard rocks (Lei et al. 2016; Lockner et al. 1991; Sellers et al. 2003). This time window was employed in the simulation.

5 Numerical results and discussions

5.1 Microcrack development

Overall, numerical simulation generated the same AE performance as the laboratory results, as shown in Fig. 7. Most AE events occurred in Stages 4 and 5. Events started to increase in Stage 4 but had a sharp increase between Stage 4 and 5. This agrees well with the crack initiation (σ_{ci}) and the crack damage (σ_{cd}) thresholds of the LdB granite. At the middle of Stage 4, both σ_1 and σ_2 exceeded σ_{ci} , but much smaller than σ_{cd} because of the high confining stress, although σ_1 reached its maximum value, as shown in Fig. 7b. The stress state produced hundreds of normally distributed microcracks (see Fig. 8) with moment magnitude below -7.0 , consistent with many laboratory experiments that stable microcracks development occurs when σ_1 exceeds σ_{ci} (Brace et al. 1966; Martin and Chandler 1993). In Stage 5, σ_1 exceeded σ_{cd} because of the quickly decreasing of σ_3 . At this stage, microcracks grew unstable (Turichshev and Hadjigeorgiou 2016), causing a sharp increase of AEs, as shown in Fig. 7a. Some cracks clustered into large AE events, as can be seen by the difference between the AE number and the microcrack number (Fig. 7a). In this stage, microcracks close to each other started to coalesce but did not form macrocracks. Therefore, AE events remained normally distribution in the

Table 3 Summary of results obtained by laboratory tests, H–B model, and numerical simulations

Properties	H–B model or laboratory test result	Simulation result	Error (%)
Tensile strength (MPa)	9.3	9.65	3.7
E (GPa)	69	69.5	0.7
UCS (MPa)	212.3	213.4	–0.3
Crack initiation strength (MPa)	75.6	79.9	5.7
Crack damage strength (MPa)	150.0	158.3	5.5
Confining pressure (MPa)	H-B strength (MPa)	Simulated strength (MPa)	Error (%)
5	285.0	309.8	8.7
10	343.8	376.5	9.5
15	395.0	429.6	8.8
20	441.2	471.6	6.9
25	483.7	499.5	3.3
30	523.4	532.2	1.7
35	560.8	557.1	–0.7
40	596.3	581.0	–2.6

sample, as illustrated in Fig. 8b. In the next three stages, few AEs occurred since σ_1 decreased to a low level.

The scattered distributed AEs in Fig. 8c disagreed with the laboratory result, which formed a potential damage plane initiating from an edge of the sample (see Fig. 3). This difference was considered to result from the end effect. In the laboratory experiment, a 4 mm chamfer was machined onto all edges of the sample to meet the edge-sealing purposes (Young et al. 2013). Therefore, loading platens were slightly smaller than the rock specimen's ends, so stress concentration occurred at the edges. The elastic mismatch between the sample and plates and the friction between them also leads to a non-uniform distribution of stress near the ends (Pan et al. 2012; Xu et al. 2017). These shortcomings caused a shear damage plane initiated from the edge and associated with the concentrated distribution of the AE events in the sample (Fig. 3c). While in the modeling, the perfect loading condition (i.e., no end and corner effects) was considered, so microcracks scattered distributed in the homogeneous rock specimen when the stress exceeds the strength of the particle contacts.

Compared to the laboratory experiment, AE events in the PFC3D modeling have higher moment magnitudes. Instant breakage of bonds in the model, as opposed to gradual bond decays in nature are known as the primary factor overestimating the moment magnitudes (Khazaei et al. 2016). Khazaei et al. (2015a) suggested that the numerical AE energies are 6.6 orders of magnitude larger than the real specimens in UCS tests when using the Gutenberg–Richter formula to calculate event magnitudes.

During the laboratory test, it is not possible to record all the events due to practical limitations. It should record many more events with magnitudes smaller than -7.0 based

on the frequency-magnitude relationship shown in Fig. 2. Events with magnitudes lower than -7.0 have a weak signal to background noise and were filtered by the monitoring system (Lockner 1993). While PFC model can record every single event, these two facts caused the numerical modeling to record many more events than the laboratory experiment.

Martin (1997) pointed out that a deviatoric stress threshold of 70–75 MPa is a reliable indicator for predicting the onset of damage near the surface of the tunnel where the confining pressure is low. However, our experiment and modeling results do not match this criterion. Deviatoric stress in Stages 6–8 is more than 100 MPa (see Fig. 1 and Table 1), but few microcracks (or AEs) occurred in these stages. In fact, damages in the tunnel crown are progressive. Damage produced in Stages 4 and 5 degrades the rock strength [deemed as cohesion loss (Martin 1997)], which promotes the subsequent damage development under the deviatoric stress criterion. Damage development will further cause strength degradation and thus damage propagation. This processing repeats and ultimately forms a notch in the roof. While in our experiment and modeling, because of the inconsistent stress path, the amount of damage in Stages 4 and 5 did not reach the level that could produce sufficient strength degradation to promote damage development. Since the LdB granite strength is sensitive to the amount of induced damage (Martin 1997), not enough damage may impose damage development in the following stages. If this progressive strength reduction processing was introduced to the PFC model, the notch formation might successfully reproduce (Potyondy and Cundall 1998).

Fig. 5 Summary of numerical results of the UCS test. **a** Particle displacement vector and AE distribution and magnitude, **b** Stress–strain curve, volumetric-strain curve, and AE number-strain curve accompanying the σ_{ci} and σ_{cd} . σ_{ci} is defined as the onset of dilatancy – increase in volume relative to elastic changes, and σ_{cd} is defined as the point of the volumetric strain reversal

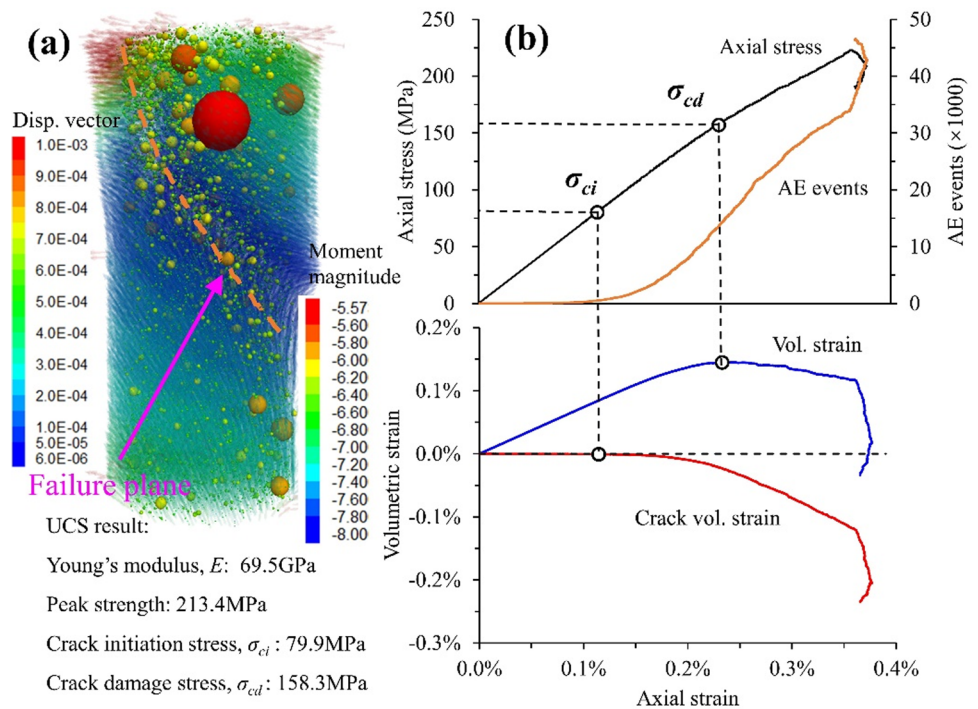
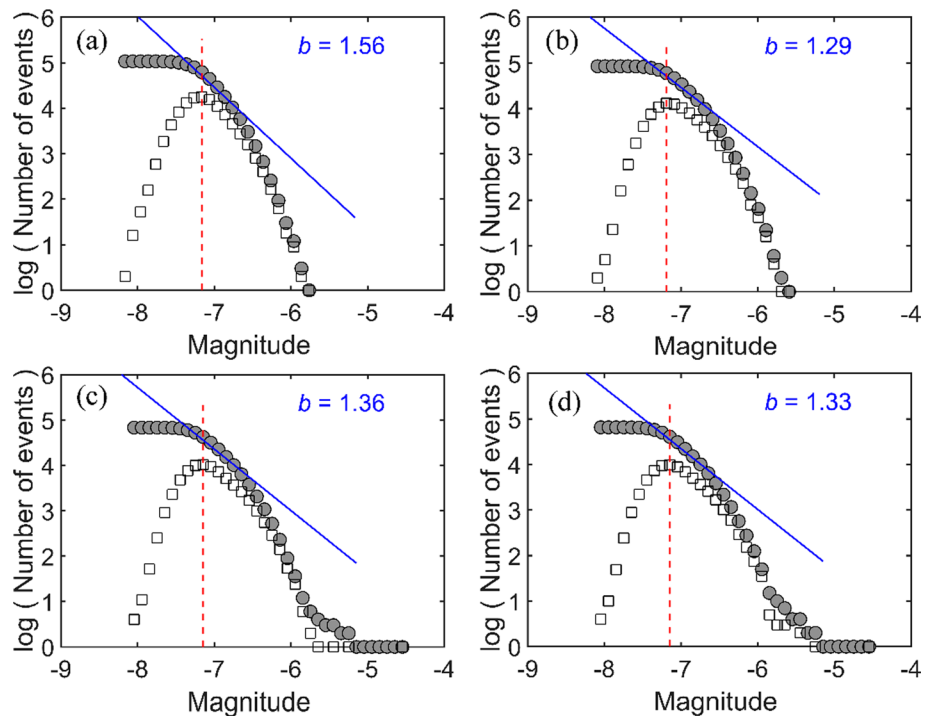


Fig. 6 Effect of TW on b -values in the UCS test. **a** 10 timestep, **b** 20 timestep, **c** 30 timestep and **d** 40 timestep. Note the low estimation quality due to the gradually curved FMD



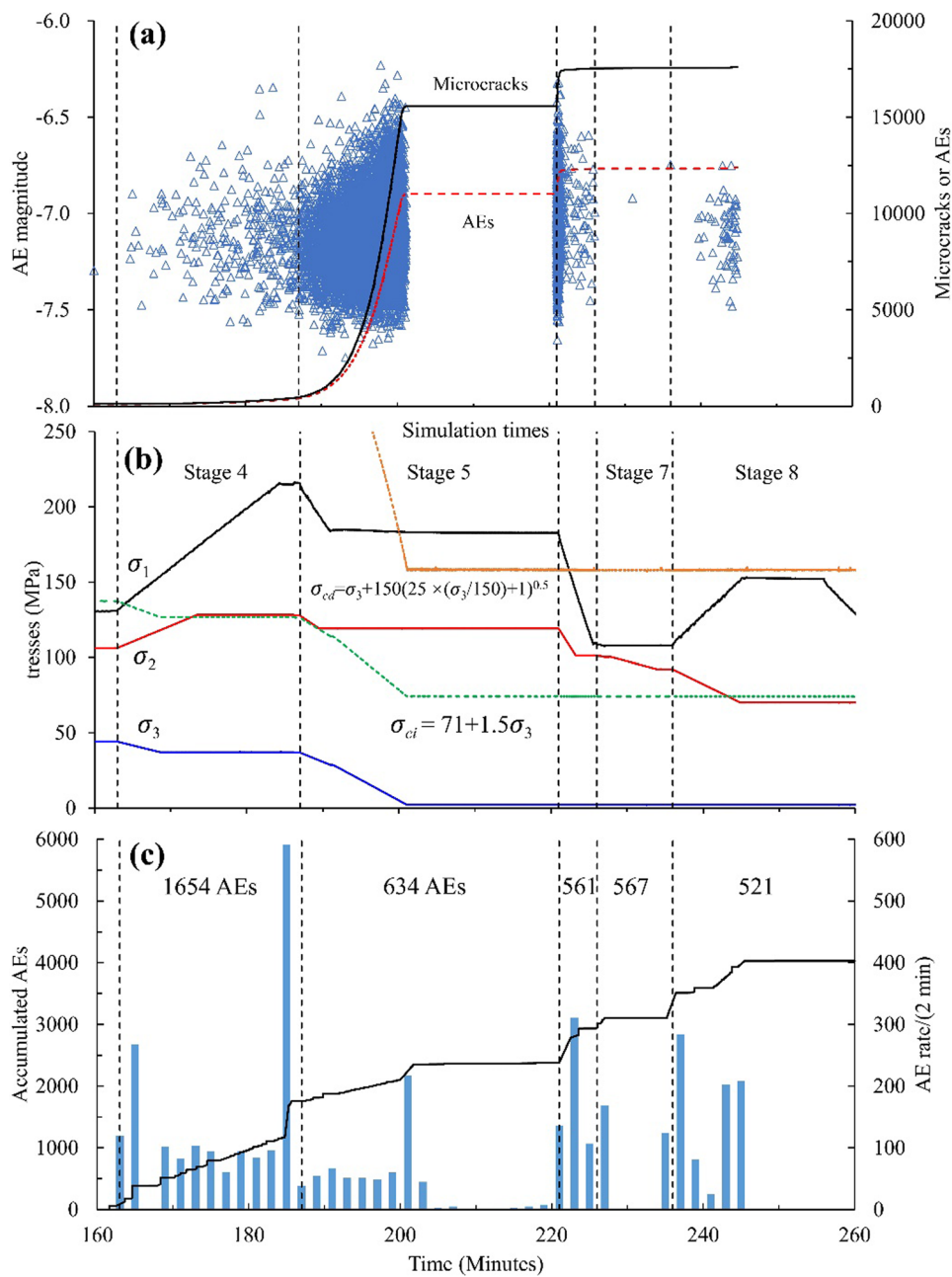
5.2 Damage mechanism

Source mechanisms in Fig. 8d show that most of the events are distributed between $-0.6 < K < 0.6$ in the Hudson diagram. These events were regarded as tensile cracks but containing a significant component of compensated linear vector dipole (CLVD). The interpretation of microseismic events

in the field also indicated that the cracking mechanism was rich in tension (Cai et al. 1998).

In the simulation, 17608 microcracks were generated. The associated stereonet is illustrated in Fig. 9, where the two dominant orientations are visible. Most microcracks are roughly parallel with σ_1 and have dip direction within 15° with respect to σ_2 . This result agrees with the major tensile

Fig. 7 Comparison of numerical simulation and the laboratory experiment. **a** Numerical AE and microcracks at different stages, **b** Principal stresses used in the test accompanying σ_{ci} (Martin 1997) and σ_{cd} (Read et al. 1998), **c** AE rate and numbers at different stages in the laboratory experiment



failure of the microcracks. Tensile cracks usually open perpendicular to σ_3 and propagate in the σ_1 - σ_2 plane.

FMD plot suggested a b -value of 1.63, as shown in Fig. 10. This result is slightly higher than the laboratory experiment result, which produced a b -value of 1.38 (see Fig. 2). The potential damage plane in the experiment should contribute to the disagreement since events clustering near the damaged plane usually produced larger events, i.e., lower b -value.

5.3 Comparison with field monitoring

AE events obtained from laboratory and numerical tests were converted to locations in relation to the tunnel face based on the relationship between stress states and distance to the tunnel face (see Table 1). Field monitoring of MSs occurring in the top-notch region in rounds 6–11 (Collins 1997) was also provided to compare with the laboratory and numerical results, as shown in Fig. 11. Overall, laboratory and numerical tests produced the same seismicity process as that monitoring in the field. In the experiment, moment

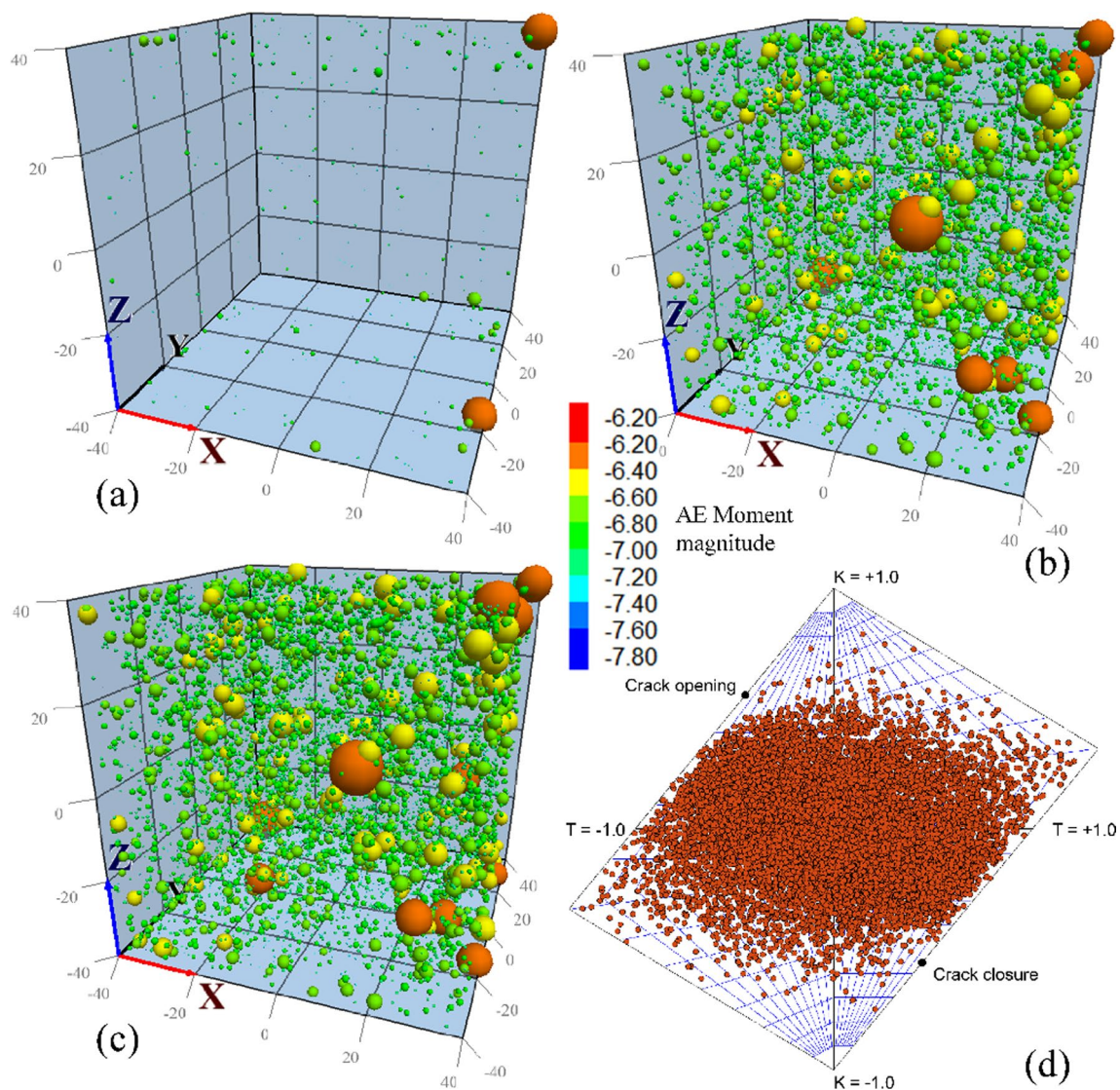


Fig. 8 Numerical simulation of cumulative AE locations at **a** Stage 4, **b** Stage 5, and **c** Stage 8 and **d** the corresponding source mechanisms

magnitudes for all the AEs are not available since only a sub-set of events are well located. Herein, the logarithm of the averaged maximum magnitude of the waveforms from an event is used to show the relative magnitude. 84.8% AE events with magnitudes > 0.0 occurred near the tunnel face. 58 events were recorded in the laboratory experiment with a distance > 1.0 m behind the tunnel face. There are 203 events (5%) occurring 8.0–10.0 m behind the tunnel face. Field monitoring and numerical simulation also obtained a few events concentrated in the region around 10 m behind the face. It is believed that the recovery of σ_1 and decreasing of σ_2 contribute to the reactivity of the events (see Fig. 7).

Experiment and simulation show that events started at the tunnel face (although several AEs occurred within

0.4 m ahead of the face), while field monitoring highlighted MSs occurring 0.7–1.4 m ahead of the active tunnel face (Collins and Young 2000; Martin 1997). It is suggested that stress rotation plays one of the significant roles in cracks occurring in front of the tunnel face (Diederichs et al. 2004; Martin 1993, 1997). Both σ_1 and σ_3 were found to rotate near the tunnel face with an angle of approximately 15° – 35° (Bai et al. 2019). Pre-existing microcracks in the rock could take advantage of stress rotations to extend in their favorable directions (Eberhardt 2001). However, only the change of stress magnitudes was considered in the laboratory and numerical simulation.

A number of seismic events happened in the region 0–2.0 m behind the tunnel face (see Fig. 11c), while these

Fig. 9 The lower hemisphere of 17608 microcrack orientations (equal area projection, Fisher concentrations). The directions of the principal stresses are indicated

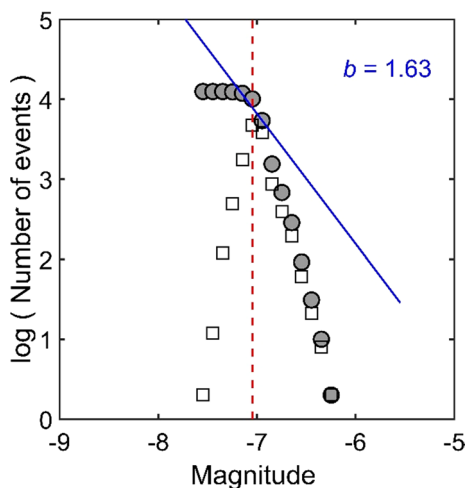
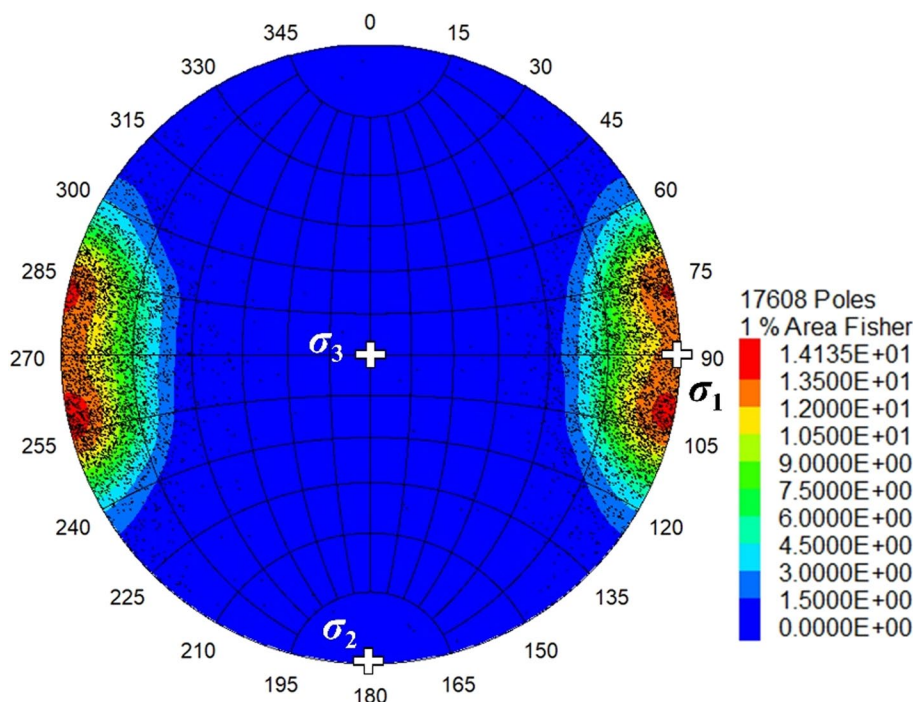


Fig. 10 Frequency-magnitude relationship plot for AE events in simulation showing a *b*-value of 1.63. Note the low estimation quality due to the gradually curved FMD

events were absent in the laboratory and numerical tests in the range 0.5–2.0 m. The different stress paths used in the tests attributed a large part to this difference. The elastic model shows that magnitude of 8.7 MPa tensile stress occurred at the crown immediately behind the tunnel face (see Fig. 1 and Table 1), which reaches the level of the tensile strength of the granite and should produce crack localization and spalling. That means the rock sample should fail if such tensile stress was applied in the laboratory and numerical test. Interpretation of microseismic events also

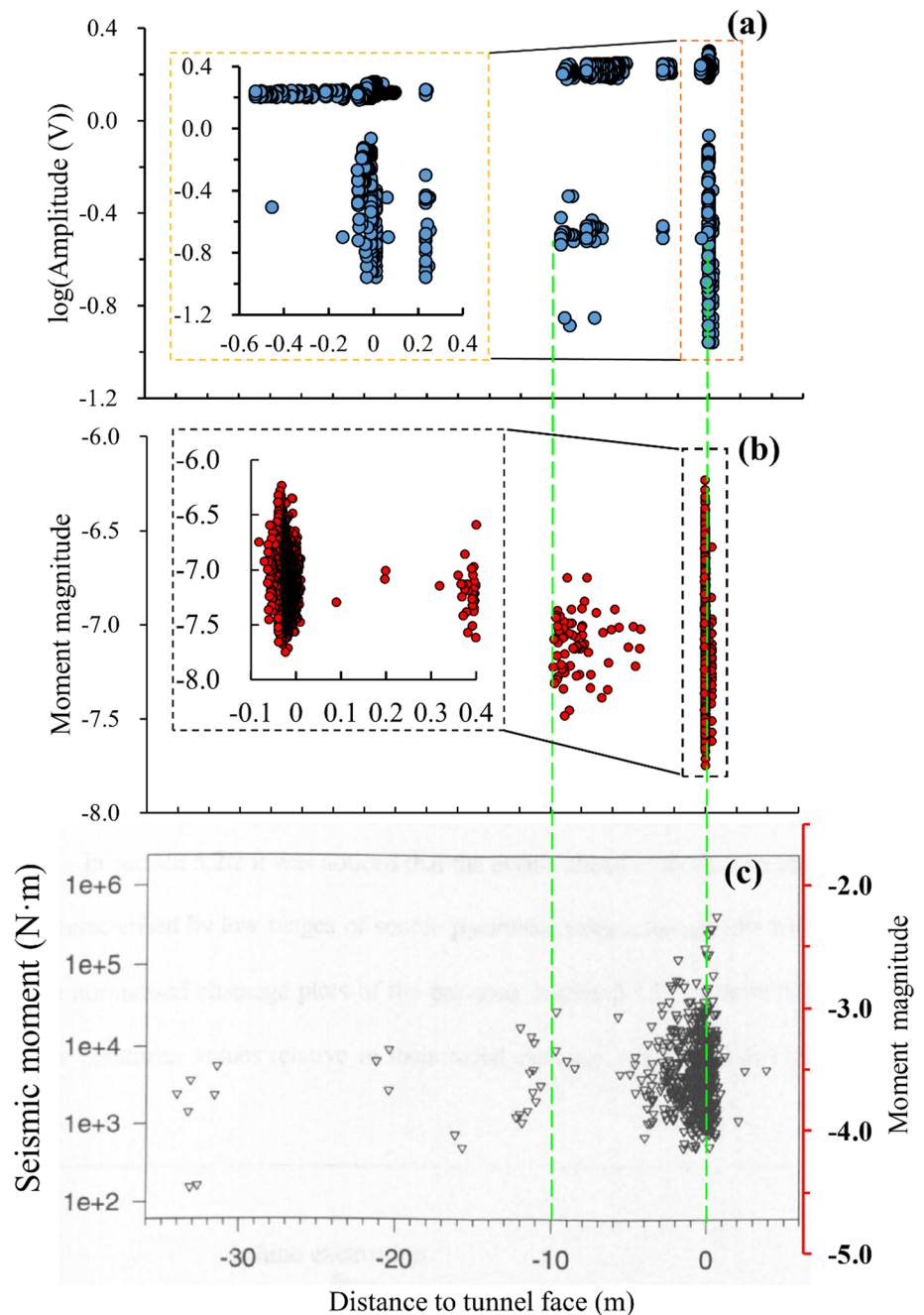
showed that cracking mechanism was rich in tension (Cai et al. 1998), and thus tensile stress dominated the failure mechanism and the fracture size. However, this tensile stress was replaced by a 2 MPa compressive stress due to the limitation of the test facility. A detailed explanation of the roles of stress rotation and tensile stress, causing the disagreements with field observations can be found in Bai et al. (2019).

Notch formation in the crown is a progressive process; after the damage initiating in front of the face, microcracks dilated, developed, slabbed, and eventually formed the stable notch (Martin 1997) in the region 0–1.5 m behind the tunnel face. This progressive process generated events continually (see Fig. 11c). Some of the interspersed nature of the large and small source radius events in the field suggest that small events are occurring first in intact rock, followed by larger events that may be connecting previously formed cracks (Collins 1997). While in our laboratory and numerical tests, preferred cracks did not occur near the face due to the inconsistent stress state (tensile stress and stress rotation). Therefore, the subsequent crack development, coalescence, and the associated seismicity were absent, and thus no macro-fractures were obtained.

5.4 Influence of intermediate principal stress

Both laboratory tests and numerical simulations show that σ_2 plays a role in rock strength, damage process, and failure mechanism (Cai 2008a; Li et al. 2015; Liu et al. 2020). However, the deviatoric stress criterion for predicting the notch

Fig. 11 The distance of events from the active tunnel face versus magnitudes for **a** Laboratory experiment, **b** Numerical model, and **c** Field monitoring (Collins 1997). The field events in **c** occurred in the upper notch region of rounds 6–11 volumes along the Mine-by tunnel, where the lithology is predominantly granite (modified from Collins (1997)). The sub-plots in **a** and **b** show the close-up near the location of 0.0 m



scale does not reflect any information of σ_2 (Martin 1997), i.e., in situ cracking starts when the maximum deviatoric stress ($\sigma_1 - \sigma_3$) exceeds approximate 70 MPa. In the numerical simulation, σ_2 was gradually decreased to the same level of σ_3 after Stage 5 to check whether σ_2 has any effect on rock damage under the specific stress path.

As predicted, both microcracks and AEs gradually increased with σ_2 decreasing, but they presented quickly growing when σ_2 is lower than 20 MPa, as shown in Fig. 12a. Overall, the increased events were uniformly distributed in the sample, as shown in Fig. 12b, which means the increased

microcracks did not coalesce into macro fractures, although many small events clustered into larger events in the sample. Note AE events result from contact breakages, and slipping on existing cracks (i.e., failed contacts) is not regarded as an event in this numerical study. The increased AEs produced a b -value of 1.55, which is lower than the original model before σ_2 decreasing (see Fig. 10), indicating more clusters of microcracks.

Most of the increased microcracks failed in tension and had a dip angle within 15° with respect to the σ_1 direction, as shown in Fig. 12c, consistent with the original state (see

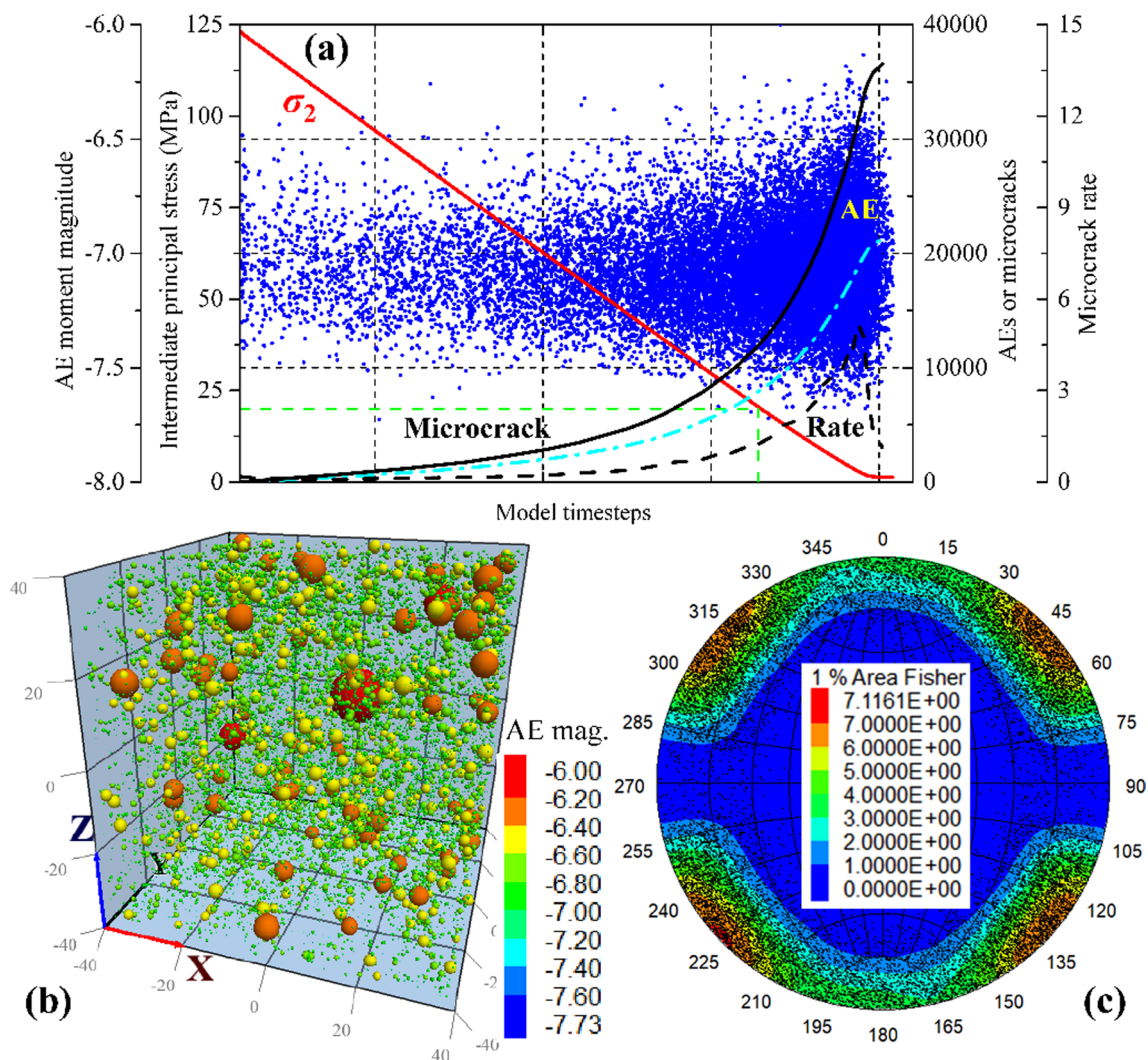


Fig. 12 **a** Increased microcracks, AE events and their magnitudes with σ_2 decreasing, **b** Distribution of the increased AEs, **c** Lower hemisphere of orientations of the microcracks (equal area projection, Fisher concentrations)

Fig. 9) before σ_2 decreasing. However, the dip direction of the microcracks is absent within 30° in relation to σ_2 . This is reasonable because most of the contacts within this direction had failed in the original state, as shown in Fig. 9.

Failure mechanism affected by σ_2 was observed in the laboratory test on hard rocks (Li et al. 2015). They found rock failure mode changed from slabbing to shear when σ_2 decreased to a critical value of 20 MPa. Our simulation also illustrates a similar mechanism. As the σ_2 unloaded, microcracks are found to incline at about 45° and 135° along the unloading direction, as the four dominant orientations are shown in the lower hemisphere figure (Fig. 12c). Because as σ_2 decreased, the orientation suppression by σ_2 was gradually weakening (Browning et al. 2017), and thus tensile microcracks turned near failed contacts where stress concentration usually occurs. However, these microcracks do not coalesce; therefore, macro shear failure was not observed

in the sample. If the unloading stopped at the 20 MPa, and σ_1 was increased to fail the sample, shear failure would be observed as illustrated in Li et al. (2015).

Detailed analysis of the microcrack development process shows that most of the generated microcracks preferred in the two orientations when σ_2 was higher than a threshold of about 20 MPa, as shown in Fig. 13. Below this threshold, failed contacts with all dip directions quickly developed. Preferred failure orientation for contacts gradually disappeared as σ_2 decreased to the same level as σ_3 , i.e., cracks generated are only parallel to the maximum principal stress and have no preferred orientation relative to σ_2 and σ_3 .

The increased AE events during σ_2 unloading highlighted that the σ_2 magnitude also affects the micro failure mechanism, which could cause different fracture mechanisms in the field. The simulation shows that lower σ_2 may produce shear failure in the roof of the Mine-by tunnel,

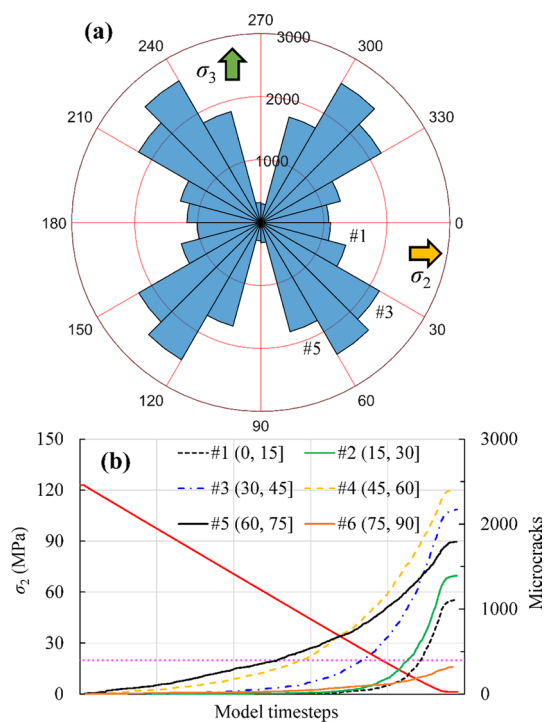


Fig. 13 **a** Orientation distribution of the microcracks during σ_2 unloading, **b** Development of microcracks for specific orientations during σ_2 unloading. The numbered orientations (e.g., #1) in plot **b** are also indicated in plot **a**

which would differ from the observed results that tensile cracking is the dominant mechanism during the notch processing (Cai et al. 1998) at the specific stress state. Also, lower σ_2 may produce larger damage zones in the roof since σ_2 unloading promotes microcracks development. Therefore, the deviatoric stress criterion for predicting the damage region in the roof (Martin 1997) also depends on σ_2 , i.e., σ_2 variance could affect the accuracy of the deviatoric stress criterion.

6 Conclusions

We have conducted a true triaxial experiment and numerical simulation on an LdB granite sample under a 3D field stress path that comes from the crown of the Mine-by tunnel. AE characteristics were investigated in the tests. In general, the numerical simulation produced the same seismicity process and AE magnitude distributions (b -value). AE events obtained from laboratory and numerical tests were converted to locations with respect to the tunnel face and were compared to the field monitoring events occurring in the top-notch region of the Mine-by tunnel. Overall, laboratory and numerical tests produced the same AE performance as monitoring in the field.

σ_2 unloading after Stage 5 reveals that microcracks continued to develop, and crack planes rotated in the direction within $30 \pm 15^\circ$ to σ_2 before it decreases to a level of 20 MPa. The concentration of the increased microcracks indicated shear damage planes may be forming during σ_2 unloading, although tensile cracks dominated in this process. Generated cracks had no preferred orientation when σ_2 was below 20 MPa. This mechanism indicated that σ_2 may play a role in damage development and should be considered when using the deviatoric stress criterion for predicting the damage region of underground excavations.

In the laboratory test, a potential damage plane that initiated from a sample edge was produced. In contrast, the micro-cracks produced in the numerical model do not indicate a possible damage plane. This disagreement may result from the stress concentration near the sample edges because the size of the loading platens is smaller than that of the rock specimen (Bai et al. 2019). Therefore, in future studies, we will conduct numerical simulations with the same boundary conditions to better reproduce the laboratory study. In this study, the tensile stress that appears near the tunnel face (see Table 1) was replaced by a compressional stress due to the limitation of the true triaxial device, which results in the different distributions of the seismic events in relation to the tunnel face (see Fig. 11). Although it is impossible to apply tensile load in the true triaxial tests, it is feasible to employ tensile boundary conditions in the numerical model. In future simulations, we will use the true stress path (including the tensile stress) to better reproduce the field observations and to better uncover the underlying mechanisms.

Acknowledgements Financial support for this study is provided by the open fund of State Key Laboratory of Coal Mine Disaster Dynamics and Control (2011DA105287-FW201901) and the National Natural Science Foundation of China (51704278). We also wish to thank Farzine Nasserri for his contributions to the laboratory experiment.

Data availability All data, models, and codes generated or used during the study are available from the corresponding author by request.

Declarations

Competing interests The authors declare that they have no competing interests.

Open Access This article is licensed under a Creative Commons Attribution 4.0 International License, which permits use, sharing, adaptation, distribution and reproduction in any medium or format, as long as you give appropriate credit to the original author(s) and the source, provide a link to the Creative Commons licence, and indicate if changes were made. The images or other third party material in this article are included in the article's Creative Commons licence, unless indicated otherwise in a credit line to the material. If material is not included in the article's Creative Commons licence and your intended use is not permitted by statutory regulation or exceeds the permitted use, you will

need to obtain permission directly from the copyright holder. To view a copy of this licence, visit <http://creativecommons.org/licenses/by/4.0/>.

References

- Aki K (1965) Maximum likelihood estimate of b in the formula $\log N = a - bM$ and its confidence limits. *Bull Earthq Res Inst Univ Tokyo* 43:237–239
- Al-Busaidi A, Hazzard J, Young R (2005) Distinct element modeling of hydraulically fractured Lac du Bonnet granite. *J Geophys Res Solid Earth* 110:B06302
- Amorèse D, Grasso J-R, Rydelek PA (2010) On varying b -values with depth: results from computer-intensive tests for Southern California. *Geophys J Int* 180:347–360
- Bahrani N, Valley B, Kaiser P et al (2011) Evaluation of PFC2D grain-based model for simulation of confinement-dependent rock strength degradation and failure processes. In: 45th US Rock mechanics/geomechanics symposium, San Francisco, USA
- Bai Q, Tu S (2019) A general review on longwall mining-induced fractures in near-face regions. *Geofluids* 2019:3089292
- Bai Q, Tibbo M, Nasser MHB et al (2019) True triaxial experimental investigation of rock response around the mine-by tunnel under an in situ 3D stress path. *Rock Mech Rock Eng* 52:3971–3986
- Bai Q, Konietzky H, Ding Z et al (2021) A displacement-dependent moment tensor method for simulating fault-slip induced seismicity. *Geomech Geophys Geo-Energy Geo-Resour* 7:79
- Brace W, Paulding B, Scholz C (1966) Dilatancy in the fracture of crystalline rocks. *J Geophys Res* 71:3939–3953
- Browning J, Meredith P, Stuart C et al (2017) Acoustic characterization of crack damage evolution in sandstone deformed under conventional and true triaxial loading. *J Geophys Res Solid Earth* 122:4395–4412
- Cai M (2008a) Influence of intermediate principal stress on rock fracturing and strength near excavation boundaries—insight from numerical modeling. *Int J Rock Mech Min Sci* 45:763–772
- Cai M (2008b) Influence of stress path on tunnel excavation response—numerical tool selection and modeling strategy. *Tunn Undergr Space Technol* 23:618–628
- Cai M, Kaiser PK, Martin CD (1998) A tensile model for the interpretation of microseismic events near underground openings. *Pure Appl Geophys* 153:67–92
- Cho N, Martin CD, Segol DC (2007) A clumped particle model for rock. *Int J Rock Mech Min Sci* 44:997–1010
- Collins DS (1997) Excavation induced seismicity in granite rock: a case study at the underground research laboratory, Canada. Ph.D Dissertation, Keele University, Staffordshire, England
- Collins DS, Young RP (2000) Lithological controls on seismicity in granitic rocks. *Bull Seismol Soc Am* 90:709–723
- Cong Y, Wang Z, Zheng Y et al (2020) Effect of unloading stress levels on macro- and microfracture mechanisms in brittle rocks. *Int J Geomech* 20:04020066
- Diederichs M, Kaiser P, Eberhardt E (2004) Damage initiation and propagation in hard rock during tunnelling and the influence of near-face stress rotation. *Int J Rock Mech Min Sci* 41:785–812
- Duan K, Kwok C (2016) Evolution of stress-induced borehole breakout in inherently anisotropic rock: insights from discrete element modeling. *J Geophys Res Solid Earth* 121:2361–2381
- Eberhardt E (2001) Numerical modelling of three-dimension stress rotation ahead of an advancing tunnel face. *Int J Rock Mech Min Sci* 38:499–518
- Eberhardt E, Stead D, Stimpson B et al (1998) Identifying crack initiation and propagation thresholds in brittle rock. *Can Geotech J* 35:222–233
- Gutenberg B, Richter CF (1944) Frequency of earthquakes in California. *Bull Seismol Soc Am* 34:185–188
- Hazzard JF, Young RP (2002) Moment tensors and micromechanical models. *Tectonophysics* 356:181–197
- Hazzard J, Young R (2004) Dynamic modelling of induced seismicity. *Int J Rock Mech Min Sci* 41:1365–1376
- Ingraham MD, Issen KA, Holcomb DJ (2013) Use of acoustic emissions to investigate localization in high-porosity sandstone subjected to true triaxial stresses. *Acta Geotech* 8:645–663
- Itasca Consulting Group Inc (2017) PFC manual, version 5.0. Itasca Consulting Group Inc, Minneapolis
- Ivars DM, Pierce ME, Darcel C et al (2011) The synthetic rock mass approach for jointed rock mass modelling. *Int J Rock Mech Min Sci* 48:219–244
- Kaiser P, Yazici S, Maloney S (2001) Mining-induced stress change and consequences of stress path on excavation stability—a case study. *Int J Rock Mech Min Sci* 38:167–180
- Khazaei C, Hazzard J, Chalaturnyk R (2015a) Damage quantification of intact rocks using acoustic emission energies recorded during uniaxial compression test and discrete element modeling. *Comput Geotech* 67:94–102
- Khazaei C, Hazzard J, Chalaturnyk R (2015b) Discrete element modeling of stick-slip instability and induced microseismicity. *Pure Appl Geophys* 173:775–794
- Khazaei C, Hazzard J, Chalaturnyk R (2016) A discrete element model to link the microseismic energies recorded in caprock to geomechanics. *Acta Geotech* 11:1351–1367
- Lei X, Funatsu T, Ma S et al (2016) A laboratory acoustic emission experiment and numerical simulation of rock fracture driven by a high-pressure fluid source. *J Rock Mech Geotech Eng* 8:27–34
- Li X, Cao W, Zhou Z et al (2014) Influence of stress path on excavation unloading response. *Tunn Undergr Space Technol* 42:237–246
- Li X, Du K, Li D (2015) True triaxial strength and failure modes of cubic rock specimens with unloading the minor principal stress. *Rock Mech Rock Eng* 48:2185–2196
- Li J, Sheng Q, Zhu Z et al (2017) Analysis of stress path and failure mode of surrounding rock during Mine-by test tunnel excavation. *Chin J Rock Mech Eng* 36:881–890
- Liu X, Feng X-T, Zhou Y (2020) Experimental study of mechanical behavior of gneiss considering the orientation of schistosity under true triaxial compression. *Int J Geomech* 20:04020199
- Lockner D (1993) The role of acoustic emission in the study of rock fracture. *Int J Rock Mech Min Sci Geomech Abstr* 30:883–899
- Lockner D, Byerlee J, Kuksenko V et al (1991) Quasi-static fault growth and shear fracture energy in granite. *Nature* 350:39–42
- Martin CD (1993) The strength of massive Lac du Bonnet granite around underground openings. Ph.D Dissertation, University of Manitoba, Winnipeg, Canada
- Martin CD (1997) Seventeenth Canadian geotechnical colloquium: the effect of cohesion loss and stress path on brittle rock strength. *Can Geotech J* 34:698–725
- Martin C, Chandler N (1993) The progressive fracture of Lac du Bonnet granite. *Int J Rock Mech Min Sci Geomech Abstr* 31:643–659
- Martin C, Read R, Martino J (1997) Observations of brittle failure around a circular test tunnel. *Int J Rock Mech Min Sci* 34:1065–1073
- Nasser M, Goodfellow S, Lombos L et al (2014) 3-D transport and acoustic properties of Fontainebleau sandstone during true-triaxial deformation experiments. *Int J Rock Mech Min Sci* 69:1–18
- Nasser MHB, Young RP, Suikkanen J (2016) ONKALO POSE experiment—strength, deformation and seismic response of Olkiluoto isotropic pegmatitic granite and anisotropic migmatitic gneiss under a state of true-triaxial stress. Posiva Oy, Eurajoki

- Pan P-Z, Feng X-T, Hudson J (2012) The influence of the intermediate principal stress on rock failure behaviour: a numerical study. *Eng Geol* 124:109–118
- Peng J, Wong LNY, Teh CI (2017) Influence of grain size heterogeneity on strength and microcracking behavior of crystalline rocks. *J Geophys Res Solid Earth* 122:1054–1073
- Potyondy D (2010) A grain-based model for rock: approaching the true microstructure. In: *Proceedings of rock mechanics in the nordic countries*, Kongsberg, Norway
- Potyondy DO (2012) A flat-jointed bonded-particle material for hard rock. In: *46th U.S. Rock mechanics/geomechanics symposium*, Chicago, America
- Potyondy DO (2015) The bonded-particle model as a tool for rock mechanics research and application: current trends and future directions. *Geosyst Eng* 18:1–28
- Potyondy DO (2017) Simulating perforation damage with a flat-jointed bonded-particle material. In: *51st US Rock mechanics/geomechanics symposium*, San Francisco, America
- Potyondy DO, Cundall PA (1998) Modelling notch-formation mechanisms in the URL Mine-by test tunnel using bonded assemblies of circular particles. *Int J Rock Mech Min Sci* 35:510–511
- Potyondy DO, Cundall PA (2004) A bonded-particle model for rock. *Int J Rock Mech Min Sci* 41:1329–1364
- Read R, Martin C (1996) Technical summary of AECL's Mine-by Experiment phase I: excavation response. Atomic Energy of Canada Ltd., Chalk River
- Read R, Chandler N, Dzik E (1998) In situ strength criteria for tunnel design in highly-stressed rock masses. *Int J Rock Mech Min Sci* 35:261–278
- Sellers EJ, Kataka MO, Linzer LM (2003) Source parameters of acoustic emission events and scaling with mining-induced seismicity. *J Geophys Res Solid Earth* 108:2148
- Tian W-L, Yang S-Q (2017) Experimental and numerical study on the fracture coalescence behavior of rock-like materials containing two non-coplanar filled fissures under uniaxial compression. *Geomech Eng* 12:541–560
- Tibbo M (2018) A true-triaxial laboratory seismic velocity experiment under in situ stress conditions: a comparison with in situ 3D stress and velocity. Ph.D Dissertation, University of Toronto, Toronto, Canada
- Turichshev A, Hadjigeorgiou J (2016) Triaxial compression experiments on intact veined andesite. *Int J Rock Mech Min Sci* 86:179–193
- Wang Y, Tonon F (2009) Modeling Lac du Bonnet granite using a discrete element model. *Int J Rock Mech Min Sci* 46:1124–1135
- Wang S, Li X, Yao J et al (2019) Experimental investigation of rock breakage by a conical pick and its application to non-explosive mechanized mining in deep hard rock. *Int J Rock Mech Min Sci* 122:104063
- Wiemer S, Wyss M (2000) Minimum magnitude of completeness in earthquake catalogs: examples from Alaska, the western United States, and Japan. *Bull Seismol Soc Am* 90:859–869
- Woessner J, Wiemer S (2005) Assessing the quality of earthquake catalogues: estimating the magnitude of completeness and its uncertainty. *Bull Seismol Soc Am* 95:684–698
- Wu S, Xu X (2016) A study of three intrinsic problems of the classic discrete element method using flat-joint model. *Rock Mech Rock Eng* 49:1813–1830
- Xu Y, Cai M, Zhang X et al (2017) Influence of end effect on rock strength in true triaxial compression test. *Can Geotech J* 54:862–880
- Xu Z, Wang W, Lin P et al (2020) A parameter calibration method for PFC simulation: development and a case study of limestone. *Geomech Eng* 22:97–108
- Yoon JS, Zimmermann G, Zang A et al (2015) Discrete element modeling of fluid injection-induced seismicity and activation of nearby fault. *Can Geotech J* 52:1457–1465
- Young RP, Nasser M, Lombos L (2013) Imaging the effect of the intermediate principal stress on strength, deformation and transport properties of rock using seismic methods, true triaxial testing of rocks. Taylor and Francis, London, pp 167–179
- Young RP, Nasser MHB, Sehzadeh M (2020) Mechanical and seismic anisotropy of rocks from the ONKALO underground rock characterization facility. *Int J Rock Mech Min Sci* 126:104190
- Zhang Z, Zhang R, Xie H et al (2016) Mining-induced coal permeability change under different mining layouts. *Rock Mech Rock Eng* 49:3753–3768
- Zhang Y, Ding X, Huang S et al (2018) Field measurement and numerical simulation of excavation damaged zone in a 2000 m-deep cavern. *Geomech Eng* 16:399–413
- Zheng G, Du Y, Cheng X et al (2017) Characteristics and prediction methods for tunnel deformations induced by excavations. *Geomech Eng* 12:361–397

Publisher's Note Springer Nature remains neutral with regard to jurisdictional claims in published maps and institutional affiliations.